Eidgenössische Technische Hochschule Zürich

Ecole polytechnique fédérale de Zurich
Politecnico federale di Zurigo
Swiss Federal Institute of Technology Zurich

Imaging acoustic obstacles by hypersingular point sources

J. Li, H. Liu*, H. Sun†, J. Zou‡

Research Report No. 2011-40
June 2011

Seminar für Angewandte Mathematik
Eidgenössische Technische Hochschule
CH-8092 Zürich
Switzerland

*Department of Mathematics, University of California, Irvine, CA 92697, USA. The work of this author is partly supported by NSF grant DMS 0724808

†Institute of Mathematics, Academy of Mathematics and Systems Science, Chinese Academy of Sciences, Beijing 100190, P. R. China

‡Department of Mathematics, The Chinese University of Hong Kong, Shatin, N. T., Hong Kong

Imaging Acoustic Obstacles by Hypersingular Point Sources

Jingzhi Li[*] Hongyu Liu[†] Hongpeng Sun[‡] Jun Zou[§]

April 3, 2011

Abstract

We investigate a qualitative method for imaging acoustic obstacles in two and three dimensions by boundary measurements. The imaging scheme makes use of the hypersingular point sources. Rigorous mathematical justification of the imaging method is established, and numerical experiments are presented to illustrate the effectiveness of the proposed imaging scheme.

1 Introduction

In this paper, we shall be concerned with an inverse boundary value problem associated with the Helmholtz equation. The problem was recently considered in [28], where the cylindrical Bessel waves are implemented to meet the imaging purpose. The cylindrical Bessel waves, $J_n(|x-y|)e^{in\hat{\phi}}$ with $x-y=|x-y|e^{i\hat{\phi}}$, are standing waves and analytic in the whole space. For the present study, we shall show that the singular point sources also fulfill the imaging/reconstruction scheme developed in [28]. The point sources are spherical wave $e^{ik|x-y|}/4\pi|x-y| = \frac{ik}{4\pi}h_0^{(1)}(k|x-y|)$ in three dimensions and the first kind Hankel function $\frac{i}{4}H_0^{(1)}(k|x-y|)$ in two dimensions. They are propagating waves and one of the most common ways in emanating waves. Point sources are easily realized in acoustics and electromagnetism, and have been widely used in engineering; see, e.g. [8]. In two dimensions, we actually could use more general point sources $\frac{i}{4}H_m^{(1)}(k|x-y|)e^{im\hat{\phi}}$ with hypersingularity, where $m \in \mathbb{N}\cup\{0\}$. Due to the singularity (or hypersingularity) of the point sources, we need to develop essentially new techniques to show that the qualitative imaging method in [28] working for analytic sources remains valid for this singular case. In the following, we shall give a brief description of the inverse problem under investigation.

[*]SAM, D-MATH, ETH Zürich, CH-8092 Switzerland. (jingzhi.li@sam.math.ethz.ch)

[†]Department of Mathematics, University of California, Irvine, CA 92697, USA. The work of this author is partly supported by NSF grant DMS 0724808. (hongyul1@uci.edu)

[‡]Institute of Mathematics, Academy of Mathematics and Systems Science, Chinese Academy of Sciences, Beijing 100190, P. R. China. (hpsun@amss.ac.cn)

[§]Department of Mathematics, The Chinese University of Hong Kong, Shatin, N. T., Hong Kong SAR. (zou@math.cuhk.edu.hk)

Consider an impenetrable scatterer D, which is the open complement of an unbounded domain of C^2 class in $\mathbb{R}^n$, $n = 2, 3$. Without loss of generality, it is assumed that the origin is contained in D. The time-harmonic acoustic wave propagation in $\mathbb{R}^n \backslash \bar{D}$ is governed by the Helmholtz equation

$$(\Delta + k^2)u = 0 \quad \text{in} \quad \mathbb{R}^n \backslash \bar{D}, \tag{1.1}$$

where u represents the wave pressure and $k > 0$ is the wave number. On the boundary of the obstacle ∂D, the wave exhibits various behaviors depending on the physical properties of the underlying obstacle. If D is *sound-soft*, one has $u|_{\partial D} = 0$; and if D is *sound-hard*, one has $\partial u/\partial \nu = 0$ on ∂D, where ν is the exterior unit normal to ∂D; whereas if D is of *impedance type*, then $\partial u/\partial \nu + i\lambda u = 0$ on ∂D, where $\lambda \in C^1(\partial D)$ is a positive function. We shall write

$$\mathcal{B}(u) = 0 \quad \text{on} \quad \partial D, \tag{1.2}$$

to denote either of the above mentioned boundary conditions or of more complicated mixed type. We emphasize that the imaging/reconstruction method developed for the inverse problem in the present paper is independent of the specific boundary condition. Actually, no *a priori* knowledge of the underlying target obstacles would be required. However, in order to ease the exposition, we stick to the case with Dirichlet boundary condition in our subsequent discussions.

In non-invasive probing, one intends to image/identify the target obstacle D by knowledge of the waves away from the object. This inverse problem forms the basis of many areas of science and technology (see e.g. [12, 24, 25] and the references therein). Many quantitative and qualitative imaging/reconstruction schemes have been developed in literature for the inverse obstacle problem; see, e.g. [2, 3, 7, 10, 11, 13, 15, 18, 20–23, 25, 26, 28, 30, 31, 33]. In [28], a qualitative imaging method is proposed following the spirit of the linear sampling method originated in [11]. The method makes use the near-field measurements encoded into the boundary Dirichlet-to-Neumann (DtN) or Neumann-to-Dirichlet (NtD) operator. A novel indicator function is developed which exhibits different behaviors depending on whether the sampling point is inside or outside the obstacle, and thus could be used to identify the shape of the underlying obstacle. It is shown in [28] that the planar or cylindrical waves could meet the reconstruction purpose. Due to the more practical feasibility, we would show that the point sources would also fulfill the imaging/reconstruction requirements. Moreover, by utilizing point sources, we actually could make use of partial wave emissions (see Section 3 for the description). We next outline the main ingredients of the scheme. Let $\Omega \subset \mathbb{R}^n$ be a bounded C^2 domain containing D such that $\Omega \backslash \bar{D}$ is connected. For the Helmholtz equation (1.1)–(1.2) confined over $\Omega \backslash \bar{D}$, we impose the following boundary condition on the exterior boundary

$$u = f \in H^{1/2}(\partial\Omega) \quad \text{on} \quad \partial\Omega. \tag{1.3}$$

It is assumed that 0 is not an eigenvalue to the problem (1.1)–(1.3). Hence, we have

a well-defined Dirichlet-to-Neumann map Λ_D defined as

$$\Lambda_D(f) = \frac{\partial u}{\partial \nu}\bigg|_{\partial\Omega}, \tag{1.4}$$

where $u \in H^1(\Omega\backslash\bar{D})$ is the unique solution to (1.1)–(1.3) and ν denotes the exterior unit normal to $\partial\Omega$. It is noted that knowing Λ_D is equivalent to knowing the Cauchy data set $(u|_{\partial\Omega}, \frac{\partial u}{\partial \nu}|_{\partial\Omega})$, which encodes the near-field wave measurements. Let $\widetilde{\Omega} \subset \mathbb{R}^n$ be a bounded C^2 domain such that $\Omega \Subset \widetilde{\Omega}$ and $\mathbb{R}^n\backslash\bar{\widetilde{\Omega}}$ is connected. Consider the following first kind integral equation

$$\int_{\partial\widetilde{\Omega}} (\Lambda_D - \Lambda_0) u(x; y) g(y) ds(y) = \frac{\partial G(x, z)}{\partial \nu(x)}, \quad x \in \partial\Omega,\ z \in \Omega \tag{1.5}$$

where $u(x; y)$ is a class of point sources located at $y \in \partial\widetilde{\Omega}$, Λ_0 denotes the DtN map without the inclusion D, and $G(x, y)$ is the Green's function for the Helmholtz equation in Ω with a vanishing Dirichlet boundary value on $\partial\Omega$. The function $g(y)$ implicitly implied in (1.5) will play the role of an indicator in identifying ∂D.

The method could be modified to making use of the NtD map. For the Helmholtz equation (1.1)–(1.2) confined over $\Omega\backslash\bar{D}$, one imposes the following boundary condition on the exterior boundary

$$\frac{\partial u}{\partial \nu} = h \in H^{-1/2}(\partial\Omega) \quad \text{on} \quad \partial\Omega. \tag{1.6}$$

Again it is assumed that 0 is not an eigenvalue to the problem (1.1)–(1.3). The NtD map Υ_D is defined by

$$\Upsilon_D(g) = u|_{\partial\Omega}, \tag{1.7}$$

where $u \in H^1(\Omega\backslash\bar{D})$ is the unique solution to (1.1), (1.2) and (1.6). The counterpart to (1.5) is given by

$$\int_{\partial\widetilde{\Omega}} (\Upsilon_D - \Upsilon_0) u(x; y) g(y) ds(y) = G_N(x, z), \quad x \in \partial\Omega,\ z \in \Omega, \tag{1.8}$$

where Υ_0 is the NtD map without the inclusion D. The function $G_N(x, z)$ is the Green's function for the Helmholtz equation on Ω with a vanishing Neumann boundary value on $\partial\Omega$.

The rest of the paper is organized as follows. In Section 2, we develop the imaging/reconstruction method based on the DtN map with point sources. In Section 3, we show that the imaging/reconstruction scheme developed also works by making use of partial wave emissions. Also, we show how to modify our imaging scheme to the case with the NtD map. Section 4 is devoted to the derivation of the explicit forms of Green's functions implemented in our method in three dimensions. In Section 5, we conducted extensive numerical experiments to illustrate the effectiveness of the proposed method.

2 Imaging by point sources with DtN map

In this section, we develop the imaging/reconstruction scheme based on the DtN map with point sources as inputs. The discussion will be addressed for point sources in three dimensions and hypersingular ones in two dimensions. As mentioned in the previous section, in three dimensions, the singular source is of the form

$$\frac{ik}{4\pi}h_0^{(1)}(k|x-y|) = e^{ik|x-y|}/4\pi|x-y|, \quad x \in \bar{\Omega},\ y \in \partial\widetilde{\Omega},$$

where $h_0^{(1)}(t),\ t \in \mathbb{R}$, is the first-kind spherical Hankel function of zeroth order; and in two dimensions,

$$w(x,y) = \frac{i}{4}H_m^{(1)}(k|x-y|)e^{im\hat{\phi}},\ x-y = |x-y|e^{i\hat{\phi}},$$

where $x = |x|e^{i\phi_x} \in \bar{\Omega}$ and $y = |y|e^{i\phi_y}$, $y \in \partial\widetilde{\Omega}$, and $H_m^{(1)}(t)$, $t \in \mathbb{R}$, is the first-kind Hankel function of mth order.

We introduce the point-source-Herglotz wave function as follows

$$(Pg)(x) := w_g(x) = \int_{\partial\widetilde{\Omega}} \frac{ik}{4\pi}h_0^{(1)}(k|x-y|)g(y)ds(y),\ g(y) \in L^2(\partial\widetilde{\Omega}), \tag{2.1}$$

where $x \in \bar{\Omega}$ and $y \in \partial\widetilde{\Omega}$. Define

$$U_{ps} := \left\{ w_g(x); w_g(x) = \int_{\partial\widetilde{\Omega}} \frac{ik}{4\pi}h_0^{(1)}(k|x-y|)g(y)ds(y),\ g(y) \in L^2(\partial\widetilde{\Omega}) \right\}. \tag{2.2}$$

We also need to introduce the Hankel-Herglotz wave function as follows

$$(Hg)(x) := w_g(x) = \int_{\partial\widetilde{\Omega}} \frac{i}{4}H_m^{(1)}(k|x-y|)e^{im\hat{\phi}}g(y)ds(y), \quad x \in \bar{\Omega}. \tag{2.3}$$

where $g(y) \in L^2(\partial\widetilde{\Omega})$, and define

$$U_h := \left\{ w_g(x); w_g(x) = \int_{\partial\widetilde{\Omega}} \frac{i}{4}H_m^{(1)}(k|x-y|)e^{im\hat{\phi}}g(y)ds(y),\ g(y) \in L^2(\partial\widetilde{\Omega}) \right\}. \tag{2.4}$$

Next, in light of the linear superposition for the Helmholtz system, we have the following two propositions.

Proposition 2.1. *Let $u(x;y) \in H^1(\Omega\backslash\bar{D})$ be the solution to the Helmholtz equation(1.1)-(1.3) associated with the Dirichlet boundary value $f(x,y) = w(x,y)|_{\partial\Omega}$ with $w(x,y) = \frac{ik}{4\pi}h_0^{(1)}(k|x-y|)$ in three dimensions and $w(x,y) = \frac{i}{4}H_m^{(1)}(k|x-y|)e^{im\hat{\phi}}$ in two dimensions. Let w_g be a Herglotz wave function (point-source or Hankel resp.). Then the solution to*

$$\begin{cases} (\Delta + k^2)u = 0 \quad in\ \Omega\backslash\bar{D} \\ u|_{\partial D} = 0, \quad u|_{\partial\Omega} = w_g|_{\partial\Omega} \end{cases} \tag{2.5}$$

is given by

$$u_g(x) = \int_{\partial\widetilde{\Omega}} u(x;y)g(y)ds(y).$$

For Proposition 2.1, we further introduce the following boundary value problem,

$$\begin{cases}(\Delta + k^2)v(x;y) = 0 \quad \text{in } \Omega\backslash\bar{D} \\ v|_{\partial D} = -f(x,y), \quad v|_{\partial\Omega} = 0\,. \end{cases} \tag{2.6}$$

It is straightforward to see that $v(x;y) = u(x;y) - w(x,y)$.

Proposition 2.2. *Let $v(x;y) \in H^1(\Omega\backslash\bar{D})$ be the solution to the Helmholtz equation (2.6) associated with the Dirichlet boundary value $f(x,y) = w(x,y)|_{\partial D}$ with $w(x,y) = \dfrac{ik}{4\pi}h_0^{(1)}(k|x-y|)$ in three dimensions and $w(x,y) = \dfrac{i}{4}H_m^{(1)}(k|x-y|)e^{im\hat{\phi}}$ in two dimensions. Let w_g be a Herglotz wave function (point-source or Hankel resp.). Then the solution to*

$$\begin{cases}(\Delta + k^2)v = 0 \quad \textit{in } \Omega\backslash\bar{D} \\ v|_{\partial D} = -w_g|_{\partial D}, \quad v|_{\partial\Omega} = 0\,. \end{cases} \tag{2.7}$$

is given by

$$v_g(x) = \int_{\partial\widetilde{\Omega}} v(x;y)g(y)ds(y).$$

Since $v(x;y) = u(x;y) - w(x,y)$ in $\Omega\backslash\bar{D}$, we note the following relation for our subsequent study

$$\left.\frac{\partial v(x;y)}{\partial\nu(x)}\right|_{\partial\Omega} = \Lambda_D(f(x,y)|_{\partial\Omega}) - \Lambda_0(f(x,y)|_{\partial\Omega}) \tag{2.8}$$

We next introduce two function spaces,

$$\begin{aligned} H^1_\Delta(\Omega\backslash\bar{D}) &:= \{u \in H^1(\Omega\backslash\bar{D});\ (\Delta + k^2)u = 0 \text{ in } \Omega\backslash\bar{D} \text{ and } u|_{\partial\Omega} = 0\}, \\ H^{-1/2}_\Delta(\partial\Omega) &:= \{\frac{\partial u}{\partial\nu}|_{\partial\Omega};\ u \in H^1_\Delta(\Omega\backslash\bar{D})\}, \end{aligned}$$

where the boundary values $\frac{\partial u}{\partial\nu}|_{\partial\Omega}$ and $u|_{\partial\Omega}$ are all understood in the sense of traces. Obviously, $H^1_\Delta(\Omega\backslash\bar{D})$ and $H^{-1/2}_\Delta(\partial\Omega)$ are both Banach spaces. Now we introduce the following two operators. Let $S : L^2(\partial\widetilde{\Omega}) \to H^1_\Delta(\Omega\backslash\bar{D})$ be defined as

$$Sg(x) := \int_{\partial\widetilde{\Omega}} v(x;y)g(y)ds(y). \tag{2.9}$$

By (2.7), we see $Sg(x)|_{\partial D} = -w_g(x)|_{\partial D}$ and $Sg(x)|_{\partial\Omega}$=0. Define $L : L^2(\partial\widetilde{\Omega}) \to H^{-1/2}_\Delta(\partial\Omega)$ by

$$Lg(x) := \int_{\partial\widetilde{\Omega}} \frac{\partial v(x;y)}{\partial\nu(x)}g(y)ds(y). \tag{2.10}$$

It is easily seen that $\dfrac{\partial Sg}{\partial\nu}(x)|_{\partial\Omega} = Lg(x)$. We are in a position to present the crucial first kind integral equation for $g_z \in L^2(\partial\widetilde{\Omega})$:

$$(Lg_z)(x) = \frac{\partial G(x,z)}{\partial\nu(x)}, \quad x \in \partial\Omega,\ z \in \Omega, \tag{2.11}$$

which by (2.8) is equivalent to (cf. equation (1.5))

$$\int_{\partial\widetilde{\Omega}}(\Lambda_D-\Lambda_0)(f(x,y))g_z(y)ds(y)=\frac{\partial G(x,z)}{\partial\nu(x)},\quad x\in\partial\Omega,\ z\in\Omega\,. \tag{2.12}$$

Here, we give a more specific description of the Green's function $G(x,z)$, $x\in\bar{\Omega}$ and $z\in\Omega$, in (2.11) and (2.12). Henceforth, we set $\Phi(x,y)=\dfrac{ik}{4\pi}h_0^{(1)}(k|x-y|)$ or $\Phi(x,y)=\frac{i}{4}H_0^{(1)}(k|x-y|)$ be respectively, the three- and two-dimensional fundamental solutions to $-\Delta-k^2$. We take $G(x,z)=\Phi(x,z)-p(x,z)$, where $p(x,z)$ is the (unique) solution to

$$(\Delta+k^2)p(x,z)=0\quad\text{in }\Omega,\quad p(x,z)|_{\partial\Omega}=\Phi(x,z)|_{\partial\Omega}, \tag{2.13}$$

for any fixed $z\in\Omega$. It is readily seen that $G(x,z)\in H^1_\Delta(\Omega\backslash\bar{D})$ if $z\in D$, and this implies $\frac{\partial G(x,z)}{\partial\nu(x)}|_{\partial\Omega}\in H_\Delta^{-1/2}(\partial\Omega)$ if $z\in D$. For the case when the artificial domain Ω is a central disk of radius $R>0$ in $\mathbb{R}^2$, an analytic expression of $G(x,z)$ is derived in Section 4, [28]. By a similar derivation, one has that if Ω is a central ball of radius $R>0$ in $\mathbb{R}^3$,

$$G(x,z)=\Phi(x,z)-\sum_{n=0}^{\infty}\sum_{m=-n}^{n}\frac{ikh_n^{(1)}(kR)j_n(k|z|)\overline{Y_n^m(\hat{z})}}{j_n(kR)}j_n(k|x|)Y_n^m(\hat{x}), \tag{2.14}$$

for $x=|x|\hat{x}\in\partial\Omega$ and $z=|z|\hat{z}\in\Omega$.

The function $g_z\in L^2(\partial\widetilde{\Omega})$ in (2.11) (or equivalently in (2.12)) shall play the key role as an indictor function in imaging/identifying ∂D, depending on whether z is inside or outside D. Indeed, we have the following theorem on the behaviors of g_z (cf. Theorem 2.5 and Remark 2.6 in [28]).

Theorem 2.3. *For g_z in (2.11) or (2.12), we have*

(i) If $z\in D$, then for every $\varepsilon>0$, there exists $g_{z,\varepsilon}\in L^2(\partial\widetilde{\Omega})$ such that

$$\|Lg_{z,\varepsilon}(x)-\frac{\partial G(x,z)}{\partial\nu(x)}\|_{H^{-1/2}(\partial\Omega)}\le\varepsilon. \tag{2.15}$$

Moreover, for every $z^*\in\partial D$ and every choice of $g_{z,\varepsilon}\in L^2(\partial\widetilde{\Omega})$ in (2.15),

$$\lim_{z\to z^*}\|g_{z,\varepsilon}\|_{L^2(\partial\widetilde{\Omega})}=\infty\quad\textit{and}\quad\lim_{z\to z^*}\|v_{g_{z,\varepsilon}}\|_{H^1(D)}=\infty. \tag{2.16}$$

(ii) If $z\in\Omega\backslash\bar{D}$, one can solve (2.11) by the Tikhonov regularization to have a regularized solution $g_{z,\varepsilon}$ in $L^2(\partial\widetilde{\Omega})$, depending on a regularizer $\varepsilon>0$. That is, $g_{z,\varepsilon}$ is the unique solution to the regularized system

$$(\varepsilon I+L^*L)\,g=L^*\frac{\partial G(\cdot,z)}{\partial\nu}\,. \tag{2.17}$$

Moreover, only one of the following two possibilities occurs to the sequence $\{g_{z,\varepsilon}\}$*: either there exists a sequence* $\varepsilon_n \to 0^+$ *such that*

$$\lim_{\varepsilon_n \to 0^+} \|Lg_{z,\varepsilon_n}(x) - \frac{\partial G(x,z)}{\partial \nu(x)}\|_{H^{-1/2}(\partial\Omega)} = 0, \tag{2.18}$$

and

$$\lim_{\varepsilon_n \to 0^+} \|g_{z,\varepsilon_n}\|_{L^2(\partial\widetilde{\Omega})} = \infty; \tag{2.19}$$

or, there exists a constant $C > 0$ *such that for all* $\varepsilon > 0$*,*

$$\|Lg_{z,\varepsilon}(x) - \frac{\partial G(x,z)}{\partial \nu(x)}\|_{H^{-1/2}(\partial\Omega)} \geq C. \tag{2.20}$$

Theorem 2.3 suggests the following procedure to determine if a point $z \in \Omega$ lies in D or not. For two cut-off values $c_1, c_2 > 0$, one first finds a Tikhonov regularized solution $g_{z,\varepsilon}$ to (2.11). If $\|g_{z,\varepsilon}\|_{L^2(\partial\widetilde{\Omega})} > c_1$, one counts $z \notin D$; Otherwise one can further compute the residual $Lg_{z,\varepsilon} - \partial G(\cdot, z)/\partial\nu$. If the norm of this residual is less than c_2, one counts $z \in D$, otherwise $z \notin D$. The above discussion leads us to the following numerical imaging/reconstruction scheme (see Fig. 1 for a schematic illustration).

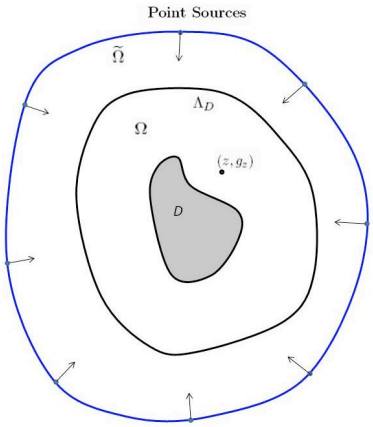

Figure 1: Schematic illustration of the imaging/reconstruction scheme by making use of the DtN map.

Numerical Imaging/Reconstruction Scheme (DtN)

Select two cut-off values $c_1, c_2 > 0$.

Step 1. Collect the measurement data $\frac{\partial u(x;y)}{\partial \nu}$ on $\partial\Omega$ corresponding to the excitation $f(x, y)$ on $\partial\Omega$ for different $y \in \partial\widetilde{\Omega}$.

Step 2. Select a sampling mesh $\mathcal{T}_h$ over the domain Ω.

Step 3. For each sampling mesh point $z \in \mathcal{T}_h$, compute a Tikhonov regularized solution $g_{z,\varepsilon}$ to (2.11).

Step 4. If $\|g_{z,\varepsilon}\|_{L^2(\partial\widetilde{\Omega})} > c_1$, we count $z \notin D$; otherwise we compute the residual $Lg_{z,\varepsilon} - \partial G(\cdot, z)/\partial\nu$. If the norm of this residual is less than c_2, we count $z \in D$; otherwise we count $z \notin D$.

The proof of Theorem 2.3 follows a similar argument to that for Theorem 2.5 in [28], provided we derive the following crucial Theorem in characterizing the operator L defined in (2.10).

Theorem 2.4. *The operator $L : L^2(\partial\widetilde{\Omega}) \to H_\Delta^{-1/2}(\partial\Omega)$ is a linear compact operator. Under the assumption that k^2 is not a Dirichlet eigenvalue for $-\Delta$ in $\Omega\backslash\bar{D}$, Ω, and D. L is injective and has a dense range in $H_\Delta^{-1/2}(\partial\Omega)$.*

In order to prove Theorem 2.4, we first show the following lemma.

Lemma 2.5. *Assume that k^2 is not a Dirichlet eigenvalue for $-\Delta$ in Ω. With respect to $H^{1/2}(\partial D)$-norm, the traces of point-source- or Hankel-Herglotz wave functions are dense in the space of traces on ∂D to the solutions of Helmholtz equation.*

Proof. In the following, we set $\Phi(x,y) = \dfrac{ik}{4\pi} h_0^{(1)}(k|x-y|)$ or $\Phi(x,y) = \frac{i}{4} H_0^{(1)}(k|x-y|)$ be respectively, the three- and two-dimensional fundamental solutions to $-\Delta - k^2$. We first prove that $U_{ps}|_{\partial\Omega}$ and $U_h|_{\partial\Omega}$ with $m = 0$ in (2.4) are dense in $H^{1/2}(\partial\Omega)$. It suffices to show that if $\varphi(x) \in H^{-1/2}(\partial\Omega)$ such that

$$\int_{\partial\Omega}\int_{\partial\widetilde{\Omega}} \Phi(x,y) g(y) ds(y) \overline{\varphi(x)} ds(x) = 0, \ \forall g \in L^2(\partial\widetilde{\Omega}), \tag{2.21}$$

then one must have $\varphi(x) = 0$. By (2.21), together with the use of Fubini's Theorem, we see

$$\int_{\partial\Omega} \Phi(x,y)\overline{\varphi(x)} ds(x) = 0 \ \text{ for } y \in \partial\widetilde{\Omega}. \tag{2.22}$$

Set

$$h(y) = \int_{\partial\Omega} \Phi(x,y)\overline{\varphi(x)} ds(x). \tag{2.23}$$

By the mapping properties of the single layer potential operator (cf.[29]), we know $h(y) \in H^1_{loc}(\mathbb{R}^n\backslash\partial\Omega)$. By (2.22), $h(y)|_{\partial\widetilde{\Omega}} = 0$. Noting $h(y)$ is a radiating solution to the Helmholtz equation in $\mathbb{R}^n\backslash\bar{\widetilde{\Omega}}$, by the uniqueness of solution to the exterior Dirichlet problem (cf. [12]), we see $h(y) = 0$ in $\mathbb{R}^n\backslash\bar{\widetilde{\Omega}}$. Further, by Unique continuation we have $h(y) = 0$ in $\mathbb{R}^n\backslash\bar{\Omega}$. In the following, we denote by γ^+ and γ^- the one-sided trace operators for Ω and $\mathbb{R}^n\backslash\bar{\Omega}$. Again by the mapping properties of single layer potential operator, we have $\gamma^- h(y) = \gamma^+ h(y) = 0$ on $\partial\Omega$. Since $(\Delta + k^2)h(y) = 0$ on Ω, and by our assumption that k^2 is not a Dirichlet eigenvalue for $-\Delta$ in Ω, we see $h(y) = 0$ on Ω. Finally, by the jump properties of the single layer potential operator (cf. [29]), we have

$$\overline{\varphi(x)} = \gamma^+ \frac{\partial h(y)}{\partial\nu} - \gamma^- \frac{\partial h(y)}{\partial\nu} = 0 \ \text{ on } \partial\Omega,$$

which proves the denseness of $U_{ps}|_{\partial\Omega}$ and $U_h|_{\partial\Omega}$ in $H^{1/2}(\partial\Omega)$. Obviously, this implies that U_{ps} and U_h are dense in the space of $H^1(\Omega)$-solutions to the Helmholtz equation, which in turn implies the result stated in the Lemma.

In like manner, for the case with hypersingular sources in two dimensions, namely U_h in (2.4) with $m \geq 1$, we only need to show that if $\varphi(x) \in H^{-1/2}(\partial\Omega)$ such that

$$\int_{\partial\Omega}\int_{\partial\widetilde{\Omega}} \frac{i}{4} H_m^{(1)}(k|x-y|)e^{im\hat{\phi}} g(y)ds(y)\overline{\varphi(x)}ds(x) = 0, \quad \forall g \in L^2(\partial\widetilde{\Omega}), \tag{2.24}$$

then one must have $\varphi(x) = 0$. Set

$$H(y) = \int_{\partial\Omega} \frac{i}{4} H_m^{(1)}(k|x-y|)e^{im\hat{\phi}}\overline{\varphi(x)}ds(x). \tag{2.25}$$

By (2.24), $H(y)|_{\partial\widetilde{\Omega}} = 0$. Since $H(y)$ is a radiating solution to the Helmholtz equation in $\mathbb{R}^2\backslash\bar{\widetilde{\Omega}}$, we see $H(y) = 0$ in $\mathbb{R}^2\backslash\bar{\widetilde{\Omega}}$ by the uniqueness of solution to the exterior Dirichlet problem. Next, let $B(0, R_1)$ be a sufficiently large central ball of radius R_1 such that $\widetilde{\Omega} \Subset B(0, R_1)$ and k^2 is not a Dirichlet eigenvalue for $-\Delta$ in $B(0, R_1)$. Moreover, we shall make use of the following addition theorem (cf. Appendix D.2, [8] or Theorem 2.12, [36]),

$$H_m^{(1)}(k|x-y|)e^{im\hat{\phi}} = \sum_{n=-\infty}^{\infty} J_{n-m}(k|x|)e^{-i(n-m)\phi_x} H_n^{(1)}(k|y|)e^{in\phi_y}, \tag{2.26}$$

for $|y| > |x|$. Clearly, we have $H(y) = 0$ for $y \in \mathbb{R}^2\backslash B(0, R_1)$. Substituting the expansion (2.26) into (2.25), we have

$$H(y)|_{\partial B(0,R_1)} = \sum_{n=-\infty}^{\infty} \frac{i}{4}\int_{\partial\Omega} J_{n-m}(k|x|)e^{-i(n-m)\phi_x}\overline{\varphi(x)}ds(x)H_n^{(1)}(k|R_1|)e^{in\phi_y} = 0. \tag{2.27}$$

Since $H_n^{(1)}(kR_1) \neq 0$, $\forall n \in \mathbb{Z}$, we further have from (2.27) that

$$\int_{\partial\Omega} J_n(k|x|)e^{in\phi_x}\varphi(x)ds(x) = 0, \ \forall n \in \mathbb{Z}. \tag{2.28}$$

Using the expansion of $H_0^{(1)}(k|x-y|)$ (cf. [8]),

$$H_0^{(1)}(k|x-y|) = \sum_{n=-\infty}^{\infty} J_n(k|x|)H_n^{(1)}(k|y|)e^{in(\phi_y-\phi_x)} \ \text{ for } |y| > |x|, \tag{2.29}$$

and multiplying $H_n^{(1)}(k|y|)e^{in\phi_y}$ to the complex conjugate of equation (2.28) and summing up for all $n \in \mathbb{Z}$, one has

$$h(y) = \int_{\partial\Omega} \frac{i}{4} H_0^{(1)}(k|x-y|)\overline{\varphi(x)}ds(x) = 0, \ y \in \mathbb{R}^2\backslash\overline{B(0, R_1)}.$$

By a similar argument to the first part of the proof, one can show that $\varphi(x) = 0$.

The proof is completed.

□

Proof of Theorem 2.4. With the help of Lemma 2.5, the compactness and denseness of the operator L can be shown by similar arguments to those for the proof of Theorem 2.3 in [28]. We only need to show the injectivity of L. Suppose $g \in L^2(\partial\widetilde{\Omega})$ and $Lg = 0$. This implies $Sg|_{\partial\Omega} = 0$ and $\frac{\partial Sg}{\partial\nu}|_{\partial\Omega} = Lg = 0$. By unique continuation, we know $Sg = 0$ in $\Omega\backslash\bar{D}$ and hence $w_g|_{\partial D} = -Sg|_{\partial D} = 0$ which further gives $w_g(x) = 0$ in D. By unique continuation again, we know $w_g = 0$ in $\widetilde{\Omega}$. Next, we divide our discussion into two cases.

For the case with singular point source $\Phi(x,y) = \dfrac{ik}{4\pi}h_0^{(1)}(k|x-y|)$ or $\dfrac{i}{4}H_0^{(1)}(k|x-y|)$, we set

$$T(x) = w_g(x) = \int_{\partial\widetilde{\Omega}} \Phi(x,y)g(y)ds(y). \tag{2.30}$$

By the mapping property of single layer potential operator, we know that $T(x) \in H^1_{loc}(\mathbb{R}^n\backslash\partial\widetilde{\Omega})$ and is a radiating solution to the Helmholtz equation in $\mathbb{R}^n\backslash\bar{\widetilde{\Omega}}$. Since $\gamma^+T(x) = \gamma^-T(x) = 0$ on $\partial\widetilde{\Omega}$, by the uniqueness of the exterior Dirichlet problem of the Helmholtz equation, we have $T(x) = 0$ in $\mathbb{R}^n\backslash\widetilde{\Omega}$. Therefore,

$$g(x) = \gamma^+\frac{\partial T(x)}{\partial\nu} - \gamma^-\frac{\partial T(x)}{\partial\nu} = 0 \ \text{ on } \partial\widetilde{\Omega}.$$

For the case with hypersingular point sources in two dimensions, we set

$$P(x) = w_g(x) = \int_{\partial\widetilde{\Omega}} \frac{i}{4}H_m^{(1)}(k|x-y|)e^{im\hat{\phi}}g(y)ds(y). \tag{2.31}$$

Choose a central disk $B(0,R_2) \Subset \widetilde{\Omega}$ of radius $R_2 > 0$, such that k^2 is not a Dirichlet eigenvalue for $-\Delta$ in $B(0,R_2)$. Plugging the expansion (2.26) into (2.31), we have

$$P(x)|_{\partial B(0,R_2)} = \sum_{n=-\infty}^{\infty}\frac{i}{4}\int_{\partial\widetilde{\Omega}} H_n^{(1)}(k|y|)e^{in\phi_y}g(y)ds(y)J_{n-m}(k|R_2|)e^{-i(n-m)\phi_x} = 0.$$

Since $J_n(kR_2) \neq 0$ for arbitrary n, we readily have from the previous equation that

$$\int_{\partial\widetilde{\Omega}} H_n^{(1)}(k|y|)e^{in\phi_y}g(y)ds(y) = 0, \quad \forall n \in \mathbb{Z}. \tag{2.32}$$

For any $x \in B(0,R_2)$, multiplying $J_n(k|x|)e^{-in\phi_x}$ to (2.32) and summing them over all $n \in \mathbb{Z}$, along with the use of the following expansion of $H_0^{(1)}(k|x-y|)$ (see [8])

$$H_0^{(1)}(k|x-y|) = \sum_{n=-\infty}^{\infty} J_n(k|x|)H_n^{(1)}(k|y|)e^{in(\phi_y-\phi_x)} \ \text{ for } |y| > |x|,$$

one has

$$\int_{\partial\widetilde{\Omega}} \Phi(x,y)g(y)ds(y) = 0 \ \text{ for } x \in B(0,R_2), \tag{2.33}$$

where $\Phi(x,y) = i/4H_0^{(1)}(k|x-y|)$. Finally, by a completely similar argument to that for the first case, one can verify directly that $g = 0$.

The proof is completed. □

3 Imaging by partial wave emissions and the NtD map

In the imaging/reconstruction scheme developed in Section 2, we have basically made use of the point sources emitted from every point lying on $\partial\widetilde{\Omega}$; see also the schematic illustration in Fig. 1. In this section, we first show that it is enough for us to make use of the point sources emitted from only part of $\partial\widetilde{\Omega}$ (see Fig. 2 for a schematic illustration). Actually, we let Γ be an open analytic arc in $\mathbb{R}^2$ or an open analytic surface in $\mathbb{R}^3$, which is an open patch of the boundary $\partial\widetilde{\Omega}$ of a bounded analytic domain $\widetilde{\Omega} \subset \mathbb{R}^n$. Then, all our study in Section 2 still hold with $\partial\widetilde{\Omega}$ replaced by Γ. We shall only outline the modified imaging/reconstruction scheme in the following.

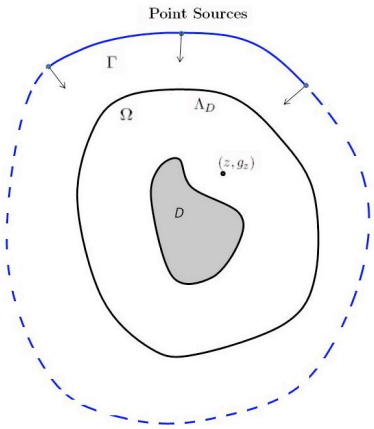

Figure 2: Schematic illustration of the imaging/reconstruction scheme with partial wave sources.

The modified indicator function $g_z \in L^2(\Gamma)$ is given by solving the following first-kind integral equation

$$\int_\Gamma (\Lambda_D - \Lambda_0)(f(x,y))g_z(y)ds(y) = \frac{\partial G(x,z)}{\partial \nu(x)}, \quad x \in \partial\Omega,\ z \in \Omega, \tag{3.1}$$

where $f(x,y)$ are the point sources as stated in Propositions 2.1 and 2.2. One can show that the modified indicator function g_z defined in this way would exhibit the same behaviors as those described in Theorem 2.3 with $\partial\widetilde{\Omega}$ replaced by Γ. To that end, it suffices to show that the modified operator L, namely the operator in (2.10) with $\partial\widetilde{\Omega}$ replaced by Γ, still possesses those properties listed in Theorem 2.4. The idea for its proof would be the same as that for Theorem 2.4 in the full emissions case, with only some slight modification in proving the denseness of the modified operator L as described in the following. In fact, for the argument of the denseness of the modified operator L, following the proof of Lemma 2.5, (2.21) becomes

$$\int_{\partial\Omega}\int_\Gamma \Phi(x,y)g(y)ds(y)\overline{\varphi(x)}ds(x) = 0,\ \forall g \in L^2(\Gamma), \tag{3.2}$$

which implies

$$\int_{\partial\Omega} \Phi(x,y)\overline{\varphi(x)}ds(x) = 0 \quad \text{for } y \in \Gamma. \tag{3.3}$$

Setting

$$h(y) = \int_{\partial\Omega} \Phi(x,y)\overline{\varphi(x)}ds(x), \quad y \in \Gamma \tag{3.4}$$

as that in (2.23). Since Γ is an open portion of the analytic boundary $\partial\widetilde{\Omega}$, we have by analytic continuation that $h(y)|_{\partial\widetilde{\Omega}} = 0$, from which one could further show that $\psi = 0$, verifying the denseness. For the two-dimensional case with hypersingular point sources, the modification would be the same.

In the rest of this section, we briefly mention the necessary modifications for all of our earlier study with the DtN map to be extended to the case with NtD map. The counterpart to (2.12) is given by

$$\int_{\partial\widetilde{\Omega}} (\Upsilon_D - \Upsilon_0)(f(x,y))g_z(y)ds(y) = G_N(x,z), \quad x \in \partial\Omega,\ z \in \Omega\,, \tag{3.5}$$

where $f(x,y) = \partial w(x,y)/\partial\nu|_{\partial\Omega}$ with $w(x,y)$ being the point-sources as stated in Propositions 2.1 and 2.2. Here, we take $G_N(x,z) = \Phi(x,z) - q(x,z)$, where $q(x,z)$ is the (unique) solution to

$$(\Delta + k^2)q(x,z) = 0 \quad \text{in } \Omega, \quad \partial q(x,z)/\partial\nu|_{\partial\Omega} = \partial\Phi(x,z)/\partial\nu|_{\partial\Omega}, \tag{3.6}$$

for any fixed $z \in \Omega$. For the case when Ω is a central disk of radius $R > 0$ in $\mathbb{R}^2$, an analytic expression of $G(x,z)$ is constructed in Section 4, [28]. By a similar construction, one can show directly that if Ω is a central ball of radius $R > 0$ in $\mathbb{R}^3$,

$$G_N(x,z) = \Phi(x,z) - \sum_{n=0}^{\infty}\sum_{m=-n}^{n} \frac{ikh_n^{(1)\prime}(kR)j_n(k|z|)\overline{Y_n^m(\hat{z})}}{j_n{}'(kR)} j_n(k|x|)Y_n^m(\hat{x}). \tag{3.7}$$

for $x = |x|\hat{x} \in \partial\Omega$ and $z = |z|\hat{z} \in \Omega$. In the following, we set

$$\widehat{S}g_z(x) := \int_{\partial\widetilde{\Omega}} (\Upsilon_D - \Upsilon_0)(f(x,y))g_z(y)ds(y), \tag{3.8}$$

and hence (3.5) becomes

$$\widehat{S}g_z(x) = G_N(x,z), \quad x \in \partial\Omega,\ z \in \Omega. \tag{3.9}$$

Under the condition that k^2 is not a Dirichlet eigenvalue to $-\Delta$ in D and Ω, it is straightforward to modify all the corresponding arguments in Section 2 to show the following theorem on the behaviors of g_z in (3.5), or equivalent in (3.9).

Theorem 3.1. *For g_z in (3.5) or (3.9), we have*

(i) If $z \in D$, then for every $\varepsilon > 0$ there exists $g_{z,\varepsilon}$ to (3.9) such that

$$\|\widehat{S} g_{z,\varepsilon}(x) - G_N(x,z)\|_{H^{1/2}(\partial\Omega)} \leq \varepsilon. \tag{3.10}$$

Moreover, for every $z^* \in \partial D$ and every choice of $g_{z,\varepsilon} \in L^2(\partial\widetilde{\Omega})$ in (3.10),

$$\lim_{z \to z^*} \|g_{z,\varepsilon}\|_{L^2(\partial\widetilde{\Omega})} = \infty \quad \text{and} \quad \lim_{z \to z^*} \|v_{g_{z,\varepsilon}}\|_{H^1(D)} = \infty. \tag{3.11}$$

(ii) If $z \in \Omega \backslash \bar{D}$, one can solve (3.9) by the Tikhonov regularization to have a regularized solution $g_{z,\varepsilon}$ in $L^2(\partial\widetilde{\Omega})$, depending on a regularizer ε. That is, $g_{z,\varepsilon}$ is the unique solution to the system

$$(\varepsilon I + \widehat{S}^* \widehat{S}) g = \widehat{S}^* G_N(\cdot, z). \tag{3.12}$$

Moreover, only one of the following two possibilities occurs to the sequence $\{g_{z,\varepsilon}\}$: either there exists a sequence $\varepsilon_n \to 0^+$ such that

$$\lim_{\varepsilon_n \to 0^+} \|\widehat{S} g_{z,\varepsilon_n}(x) - G_N(x,z)\|_{H^{1/2}(\partial\Omega)} = 0 \tag{3.13}$$

and

$$\lim_{\varepsilon_n \to 0^+} \|g_{z,\varepsilon_n}\|_{L^2(\partial\widetilde{\Omega})} = \infty\,; \tag{3.14}$$

or, there exists a positive constant C such that for all $\varepsilon > 0$,

$$\|\widehat{S} g_{z,\varepsilon}(x) - G_N(x,z)\|_{H^{1/2}(\partial\Omega)} \geq C. \tag{3.15}$$

Based on Theorem 3.1, the imaging/reconstruction scheme using the NtD map is given as follows.

Numerical Imaging/Reconstruction Scheme (NtD)

Select two cut-off values $c_1, c_2 > 0$.

Step 1. Collect the measurement data $u(x; y)$ on $\partial\Omega$ corresponding to $\partial w(x,y)/\partial\nu$ on $\partial\Omega$ for different $y \in \partial\widetilde{\Omega}$.

Step 2. Select a sampling mesh $\mathcal{T}_h$ over the domain Ω.

Step 3. For each sampling point $z \in \mathcal{T}_h$, compute a Tikhonov regularized solution $g_{z,\varepsilon}$ to the equation (3.9).

Step 4. If $\|g_{z,\varepsilon}\|_{L^2(\partial\widetilde{\Omega})} > c_1$, we count $z \notin D$; otherwise we compute the residual $\widehat{S} g_{z,\varepsilon_n}(x) - G_N(x,z)$. If the norm of this residual is less than c_2, we count $z \in D$; otherwise we count $z \notin D$.

Finally, we would like to mention that the previous study for imaging/reconstruction with NtD map could be equally extended to the case with only partial wave emissions. The extension would be the same as that described in the first part of the present section for the case with DtN map, and we would not repeat it.

4 Numerical experiments and discussions

In this section, numerical experiments are presented to illustrate applicability and effectiveness of the new imaging/resonctruction approach developed in the previous sections for the inverse obstacle scattering by near fields in two and three dimensions. Some key parameters are fixed as follows: $R = 5.5$ for the radius of the surrounding disk Ω, $R_1 = 6.5$ for the radius of fictitious disk $\widetilde{\Omega}$ in two dimensions (ball in three dimensions, resp.), $k = 1$ for the wave number, $m = 3$ for the order of hypersingular point sources in two dimensions, $\delta = 1\%$ for the noise level, and $c = (c_x, c_y)^T$ for the object shifting with displacements c_x and c_y from the origin in two dimensions.

In the sequel, all the synthetic near-field data of the direct problems are generated by solving the variational equation corresponding to the system (1.1)-(1.2) with isoparametric quadratic finite elements and encoded as the NtD map, which measure the potential data u given the exact known Neumann input data, does not require approximate differentiation of the potential data u for the Neumann data on the boundary in the DtN map case and thus avoid possible instability due to the synthetic data. We solve the discrete system over a family of increasingly finer meshes over the computational domain $\Omega \setminus D$ until the relative error is small, e.g., less than 10^{-3}, which, compared with the noise level we added, is negligible and viewed as noise-free measurement data. The near-field data generated on the boundary $\partial\Omega$ are then subjected pointwise to certain uniform random noise. The uniform random noise in magnitude as well as in direction is added according to the following formula,

$$U = U + \delta\, r_1 |U| \exp(i\pi\, r_2)\,, \tag{4.1}$$

where U may be the measurement data from u or $\frac{\partial u}{\partial \nu}$, r_1 and r_2 are two uniform random numbers, both ranging from -1 to 1, and δ represents the noise level. For each mesh point z, the corresponding integral equation is discretized through the midpoint quadrature rule at the equidistantly distributed collocation points along the boundary $\partial\Omega$ in two dimensions, or transformed in the spherical coordinate system for spherical quadrature with equally spaced nodes in both latitudinal and longitudinal directions in three dimensions. Afterward, the linear system is solved by using the Tikhonov regularization technique, with the corresponding regularization parameters determined by the generalized Morozov discrepancy principle.

For obstacle imaging in two dimensions, we shall test three different scatterers: a unit disk of radius 1, a kite-shaped object, which are denoted by **Di** and **K**, respectively, and a combination of **Di** and **K** (possibly at different locations). These scatterers can be parameterized as follows:

$$\texttt{Disk:} \qquad x(t) = (\cos t, \sin t), \quad 0 \le t \le 2\pi, \tag{4.2}$$

$$\texttt{Kite:} \qquad x(t) = (\cos t + 0.65\cos 2t - 0.65, 1.5\sin t), \quad 0 \le t \le 2\pi. \tag{4.3}$$

In two dimensions, the measurement data depend on two variables: the observation location x on the medium boundary Γ and the incident direction d from the unit circle in $\mathbb{R}^2$, where we write $x = (R\cos(\phi), R\sin(\phi))$ with $\phi \in [-\pi, \pi]$, and $d =$

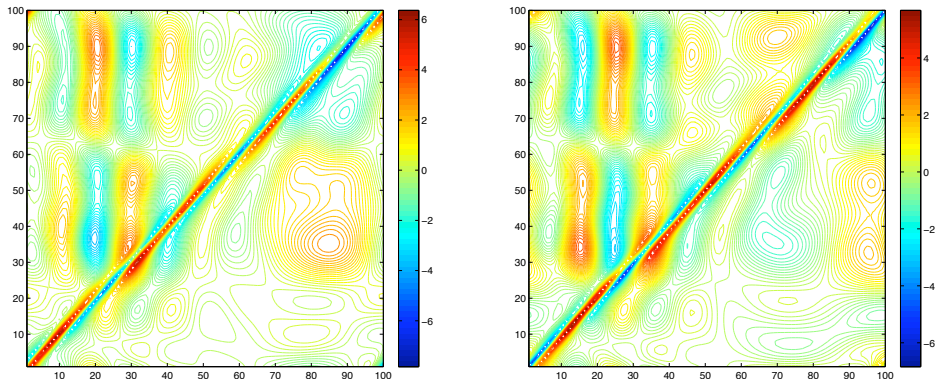

(a) (b)

Figure 3: Contour plots of the real part (a) and imaginary part (b) of the observation data u with the hypersingular wave with no noise in Example 1.

$(\cos(\theta), \sin(\theta))$ with $\theta \in [-\pi, \pi]$. We compute the near-field measurement data at 100 equidistantly distributed observation points $x_j = (R\cos\phi_j,\ R\sin\phi_j)$, $\phi_j = 2j\pi/100 - \pi$, $j = 1, 2, \ldots, 100$, corresponding to 100 equidistantly distributed incident directions $d_j = (\cos\theta_j, \sin\theta_j)$, $\theta_j = 2j\pi/100 - \pi$, $j = 1, 2, \ldots, 100$, around the surrounding medium circle. We may identify the observation points and incident directions with the index sequence $\{1, 2, \ldots, 100\}$ and illustrate the measurement data by the contour plots of the corresponding 100×100 matrices as shown in the following examples. Hereafter, the norms of the indicator function g_z and the residual of the integral equation $\frac{\partial G(x,z)}{\partial \nu(x)} - Lg_z$ in the NtD case are denoted by *g-norm* and the *res-norm*, respectively. Furthermore, these norms are plotted by transformation via 10-based logarithm for better visualization.

Example 1. Unit disk obstacle with $c = (-1.5, -1.5)^T$.

Figure 3 shows the contour plots of the real and imaginary parts, respectively, of the near-field potential data u. In both plot, we see that the matrices have significantly larger entries around their anti-diagonal. which is due to the highly localized hypersingular source term. Except very few clues like anti-diagonal dominant pattern, it is very hard to envisage the shape of the obstacle. The imaging problem we are confronted with is to reconstruct the unknown obstacle from those elusive measurement data.

We show the contour plot of the g-norm indicator function in Figure 4(a) and the buried unit disk can be approximately reconstructed with the cut-off value V_{cut} chosen to be -0.127 as shown in Figure 4(b). For the res-norm case, the contour plot and the identified object with the cut-off value V_{cut} chosen to be -2.03 are shown in Figure 4(c) and (d), respectively. It is interesting that both indicator functions (g-norm or res-norm) work well for this example and the unknown object can soundly detected with correct location and approximate shape and size. The blow-up behavior of the g-norm, predicted by our theoretical result, is clearly shown in Figure 4(a) . The res-norm indicator function also reveals a pattern of blow-up, which has never been

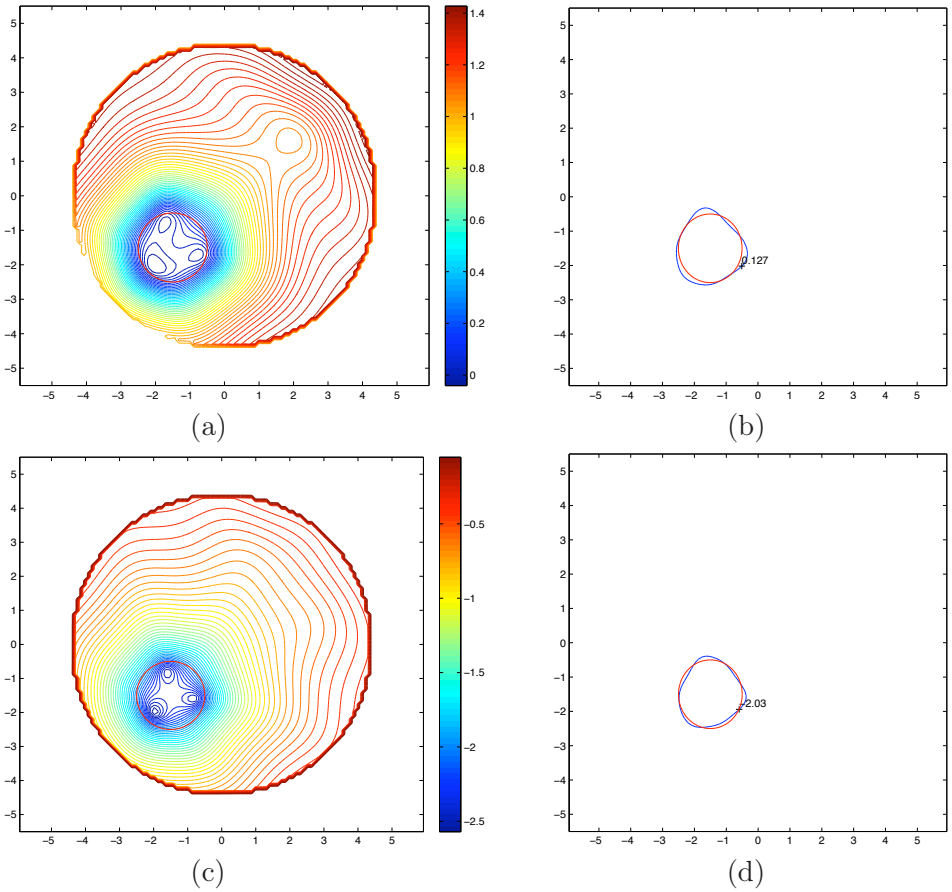

Figure 4: Example 1. Contour plots of the g-norm indicator (a) and res-norm indicator (c). Reconstructed obstacles from the g-norm (b) and res-norm (d) with the reference obstacle in the red line and reconstructed one in the blue line.

investigated before and and make a distinct difference for obstacle imaging problems between using near-field and far-field data. More precisely, one has two groups of indicator functions which can be both used for imaging/reconstruction.

It is pointed out that the choice of the cut-off value is crucial for the reconstruction. The same idea from [27] can be extended here for the determination of cut-off values for obstacle imaging/resonctruction problems by taking advantage of the mutual interaction between obstacle components. We will further demonstrate the effectiveness of such choice scheme with the multi-component obstacle case in Example 3.

***Example* 2.** Kite obstacle with $c = (0, 0)^T$.

We test a non-convex kite-shaped obstacle in this example. Figure 5 shows the contour plots of the real and imaginary parts, respectively, of the near-field potential data u. From the contour plots of the g-norm and res-norm indicator functions in Figure 6(a) and (c), respectively, the obstacle can be imaged/reconstructed by choosing the cut-off values V_{cut} to be 0.159 and -1.91, respectively, as shown in Figure 6(b)

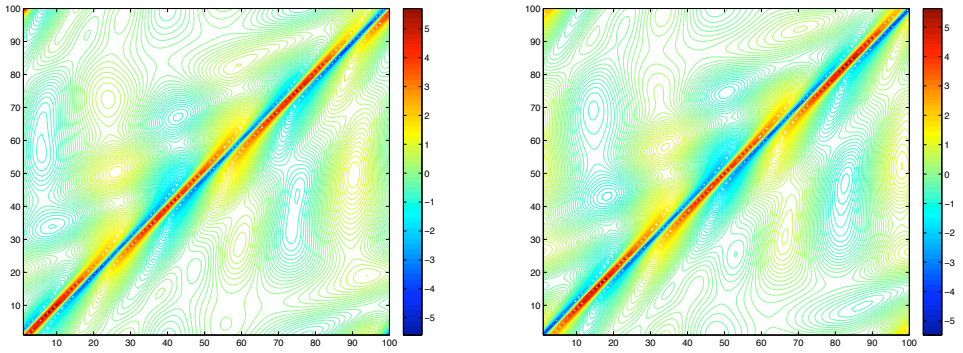

(a) (b)

Figure 5: Contour plots of the real part (a) and imaginary part (b) of the observation data u with the hypersingular wave with no noise in Example 2.

and (d), respectively. In particular the non-convex part is approximated very well, which shows that our reconstruction algorithm is a promising imaging scheme for even non-convex obstacles. We see again that the res-norm reconstruction performs better than the g-norm one, which is exaggerated to the left tip part.

For this kite example, we investigate the possibility of using partial point source emission waves for imaging purpose. The emission angle is reduced from the full range $[-\pi, \pi)$ (full circle) to $[-\pi, 0]$ (lower half circle in the third and fourth quadrants), and then further to $[-\pi/2, 0]$ (lower right quarter circle in the fourth quadrant). For partial emission waves from lower half circle, we see in Figure 7 that the lower part of the kite is better reconstructed than its upper part, in particular in the lower left wing tip of the kite. Compared with full-range emission case, the obstacle is more deformed due to the lack of full data while the shape of the kite is still identifiable using half of the measurement data. When the emission range is further restricted on the lower right quarter circle in the fourth quadrant, Figure 8 tells us that only the rough location of the kite and the lower part facing the emission angles can be reasonably approximated, and the upper left part of the kite cannot be imaged well due to the severe lack of very limited data and the fast decay properties of hypersingular point sources. This example verifies our claim in Section 3 and endows practitioners with the chance to obtain rough image information based on limited emission waves, for instance, in case that only location and crude shape are preferred, such as mine detection..

***Example* 3.** A combination of disk and kite obstacles with $c_{disk} = (-2, -2)$ and $c_{kite} = (2, 2)^T$.

In this example, we test the multi-component obstacle case with a combination of a unit disk and a kite with some displacement. Figure 9 shows the contour plots of the real and imaginary parts, respectively, of the near-field potential data u.

On the one hand, due to strong interaction from the close distance, those parts of different objects facing each other are attracted to a certain degree, which causes those parts looks a bit deformed. Nevertheless, the identified object is still a reasonable ap-

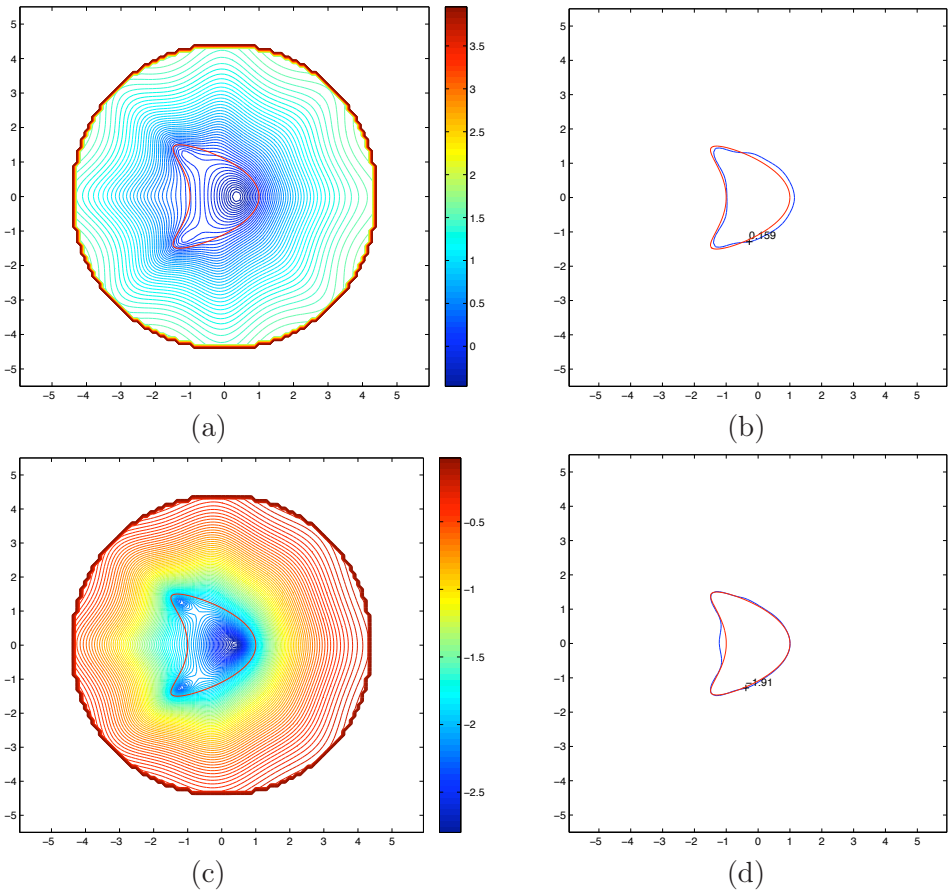

Figure 6: Example 2. Contour plots of the g-norm indicator (a) and res-norm indicator (c). Reconstructed obstacles from the g-norm (b) and res-norm (d) with the reference obstacle in the red line and reconstructed one in the blue line.

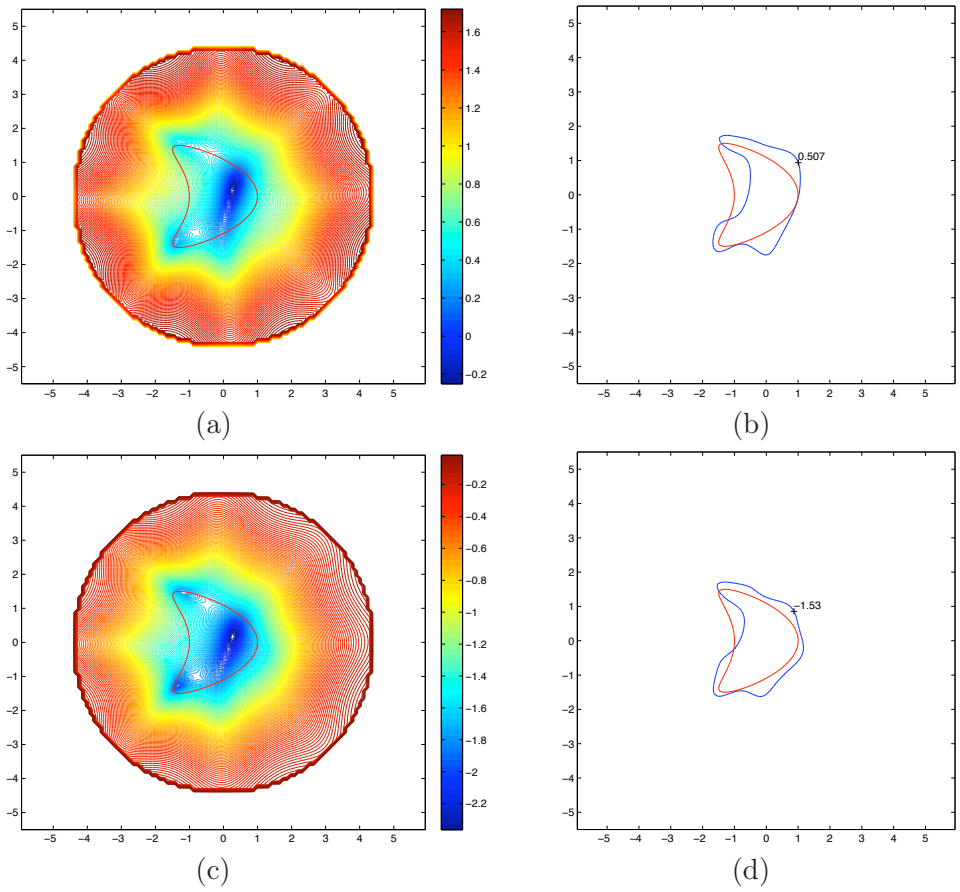

Figure 7: Example 2 with partial emission waves from lower half circle in the third and fourth quadrants. Contour plots of the g-norm indicator (a) and res-norm indicator (c). Reconstructed obstacles from the g-norm (b) and res-norm (d) with the reference obstacle in the red line and reconstructed one in the blue line.

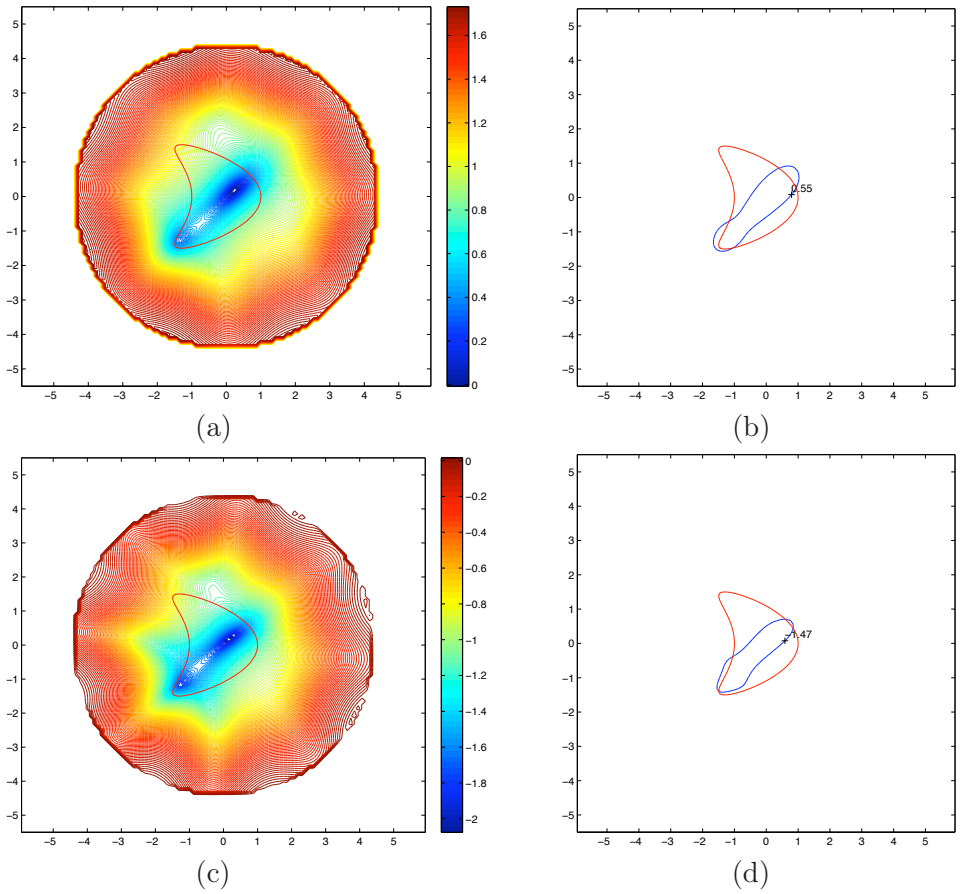

Figure 8: Example 2 with partial emission waves from lower left quarter circle in the fourth quadrant. Contour plots of the g-norm indicator (a) and res-norm indicator (c). Reconstructed obstacles from the g-norm (b) and res-norm (d) with the reference obstacle in the red line and reconstructed one in the blue line.

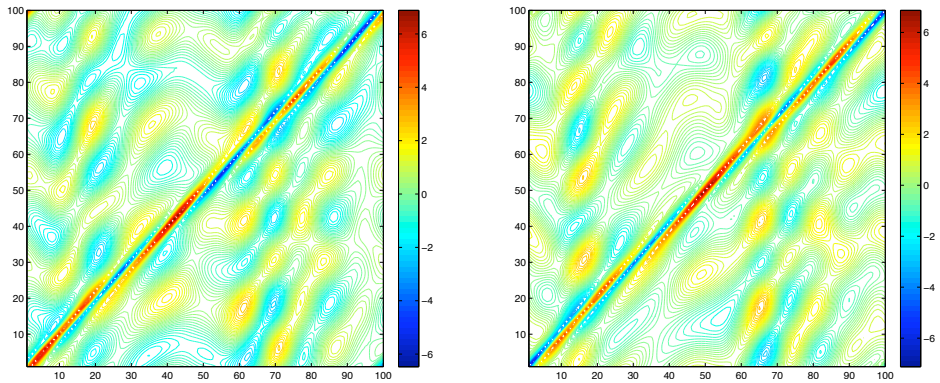

(a) (b)

Figure 9: Contour plots of the real part (a) and imaginary part (b) of the observation data u with no noise in Example 3.

proximation of the original multi-component unknown obstacle. We show the contour plot of the g-norm indicator function in Figure 10(a) and the multi-component obstacle can be approximately reconstructed with the cut-off value V_{cut} chosen to be 0.182 as shown in Figure 10(b). For the res-norm case, the contour plot and the identified object with the cut-off value V_{cut} chosen to be -2.47 are shown in in Figure 10(c) and (d), respectively. In this example, the reconstruction based on the g-norm indicator seems better than that based on the res-norm, particularly for those parts facing each other.

On the other hand, this example can be explained in an alternative way, namely it provides a similar reference idea as in [27] to choose the cut-off value in the near-field obstacle imaging problems, which is in light of the mutual interaction between the components of the objects. In this example, the unit disk can be used as a reference object a priori known, we may read out the cut-off value from the isoline which matches best the known component, and then use it to plot the isoline with the same cut-off value to recover the unknown kite component, and vice verse. We see clearly that the cut-off values of the two objects are correlated with each other due to the mutual interaction of wave between the objects. Furthermore, those parts of objects facing each other are slightly attracted due to much stronger interaction effects with smaller distance between those parts.

Lastly, for obstacle imaging in three dimensions, we test two examples in the three-dimensional case. The scatterers are chosen, respectively, a unit ball centered at the origin and an acorn parametrized by $\rho^2(\theta) = \frac{9}{25}(\frac{17}{4} + 2\cos(3\theta))$ evolving around the z-axis [12, 14], as shown in Figures 11(a) and 12(a). For three-dimensional problems, the observed data are measured in 41×41 pairs of equally-spaced latitudinal and longitudinal coordinates on the surrounding sphere $\partial\Omega$ with point source waves emitted from 41×41 pairs of equally-spaced latitudinal and longitudinal directions.

***Example* 4.** Unit ball obstacle centered at the origin.

The computational region is approximated by triangulation in Figures 11(b). Fig-

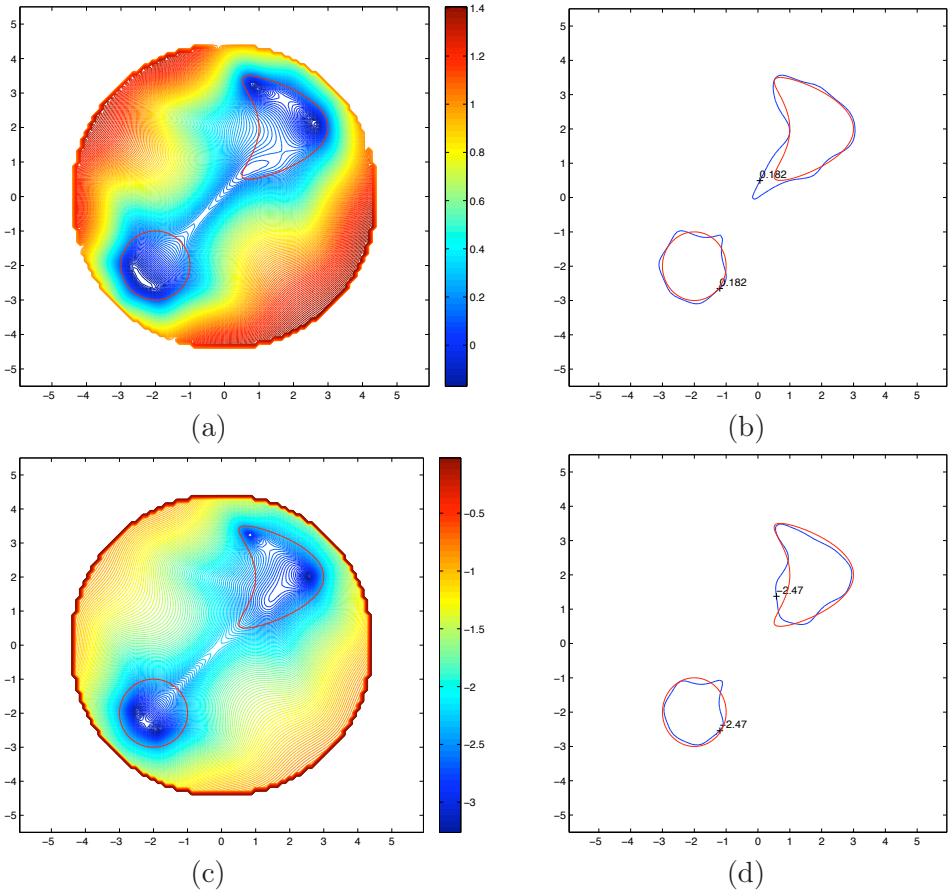

Figure 10: Example 3. Contour plots of the g-norm indicator (a) and res-norm indicator (c). Reconstructed obstacles from the g-norm (b) and res-norm (d) with the reference obstacle in the red line and reconstructed one in the blue line.

ures 11(c) and (d) illustrate one sample of the observed data u for the unit ball scatterer when the singular source point is located at $y = (-R_1, 0, 0)$. The unit ball serves as a calibration of the method. To that end, we extract an isosurface with the cutoff value 0.142 from the g-norm indicator in Figure 11(e) and the other isosurface with the cutoff value -0.8157 from the res-norm indicator in Figure 11(f).

***Example* 5.** Acorn obstacle.

The last example is a three-dimensional nonconvex scatterer, and the computational region is approximated by triangulation in Figures 12(b). Figures 12(c) and 12(d) illustrate a sample image of the real and imaginary parts of the observed data u for the acorn scatterer when the source point is located at $y = (-R_1, 0, 0)$. Figures 12(e) and 12(f) show the reconstructed shapes for the acorn with the g-norm and res-norm indicators, respectively, with cut-off value being 0.098 and -0.632. The location, shape and size of the reconstructed object are all well approximated if noise is taken into account. Once again, this example demonstrate the applicability of the indicators to determine an reasonably approximated unknown obstacle for practical use in three dimensions.

References

[1] Abramowitz, M. and Stegun I. A., *Handbook of Mathematical Functions*, New York: Dover Publications, 1965

[2] Ammari, H., Griesmaier, R. and Hanke, M., *Identification of small inhomogeneities: Asymptotic factorization*, Math. Comp., **76** (2007), 1425–1448.

[3] Arens, T., *Why the linear sampling method works*, Inverse Problems, **20** (2004), 163–173.

[4] Cakoni, F. and Colton, D., *Qualitative Methods in Inverse Scattering Theory*, Springer, 2006.

[5] Cavicchi, T. J. and O'Brien, W. D. Jr., *Acoustic sacttering of an incident cylindrical wave by an infinite circular cylinder*, IEEE Trans Ultrason. Ferroelectr. Freq. Control, **35** (1988), 78–80.

[6] Chen, Y., *Inverse scattering via skin effect*, Inverse Problem, **13**(1997), 647–667.

[7] Cheney, M., *The linear sampling method and the MUSIC algorithm*, Inverse Problems, **17** (2001), 591-595.

[8] Chew, W. C., *Waves and Fields In Inhomogenenous Media*, Van Nostrand Reinhold, 1990.

[9] Colton, D. and Haddar, H., *An application of the reciprocity gap functional to inverse scattering theory*, Inverse Problems, **21** (2005), no. 1, 383–398.

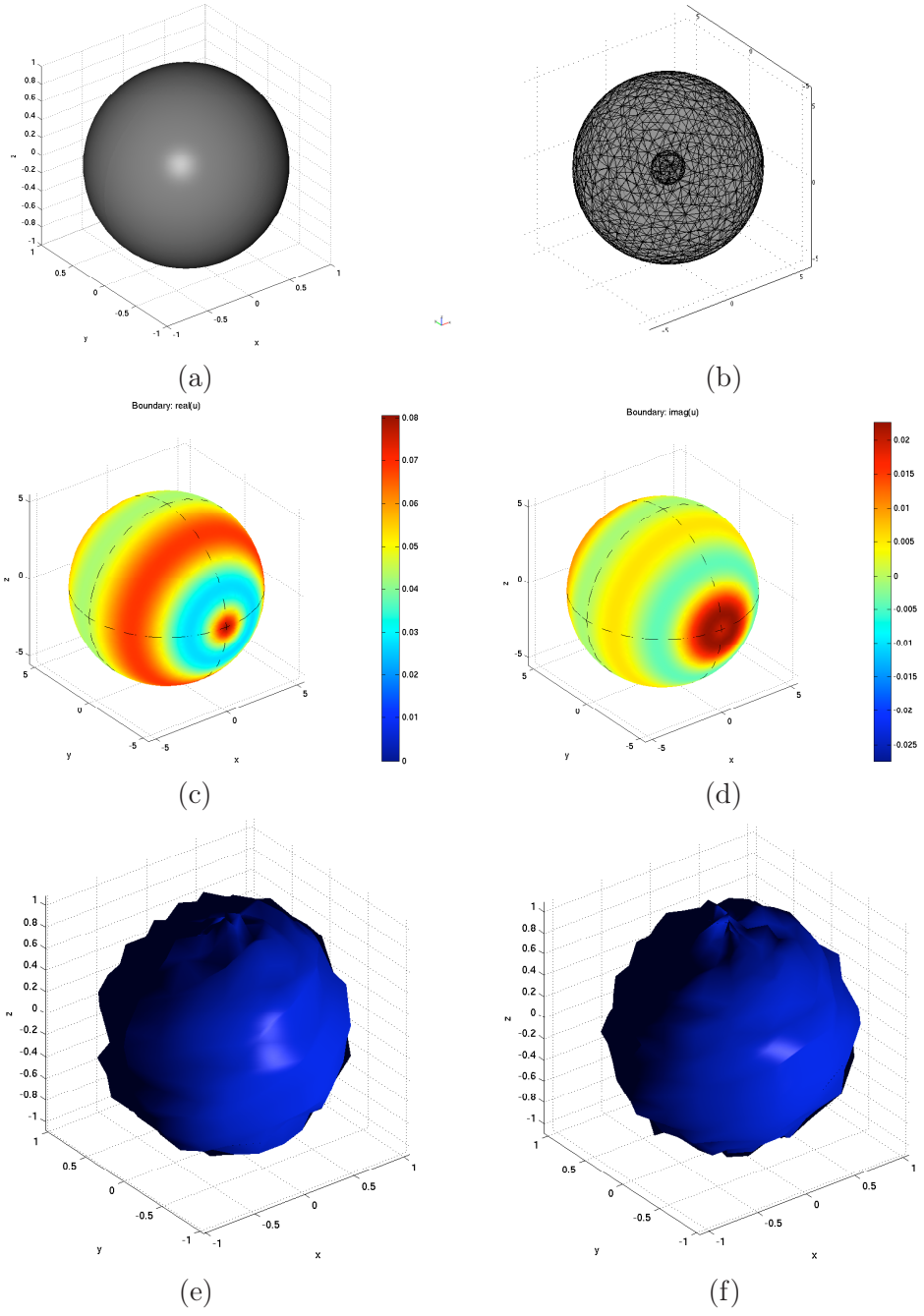

Figure 11: Example 4 with the singular point source. Exact shape of the unit sphere (a) and triangulation (b). Observed data u on the boundary of the surrounding sphere in real (c) and imaginary (d) parts when the singular source is located at $y = (-R_1, 0, 0)$. Reconstructed obstacles from the g-norm (e) ($V_{cut} = 0.142$) and res-norm (f) ($V_{cut} = -0.815$), respectively.

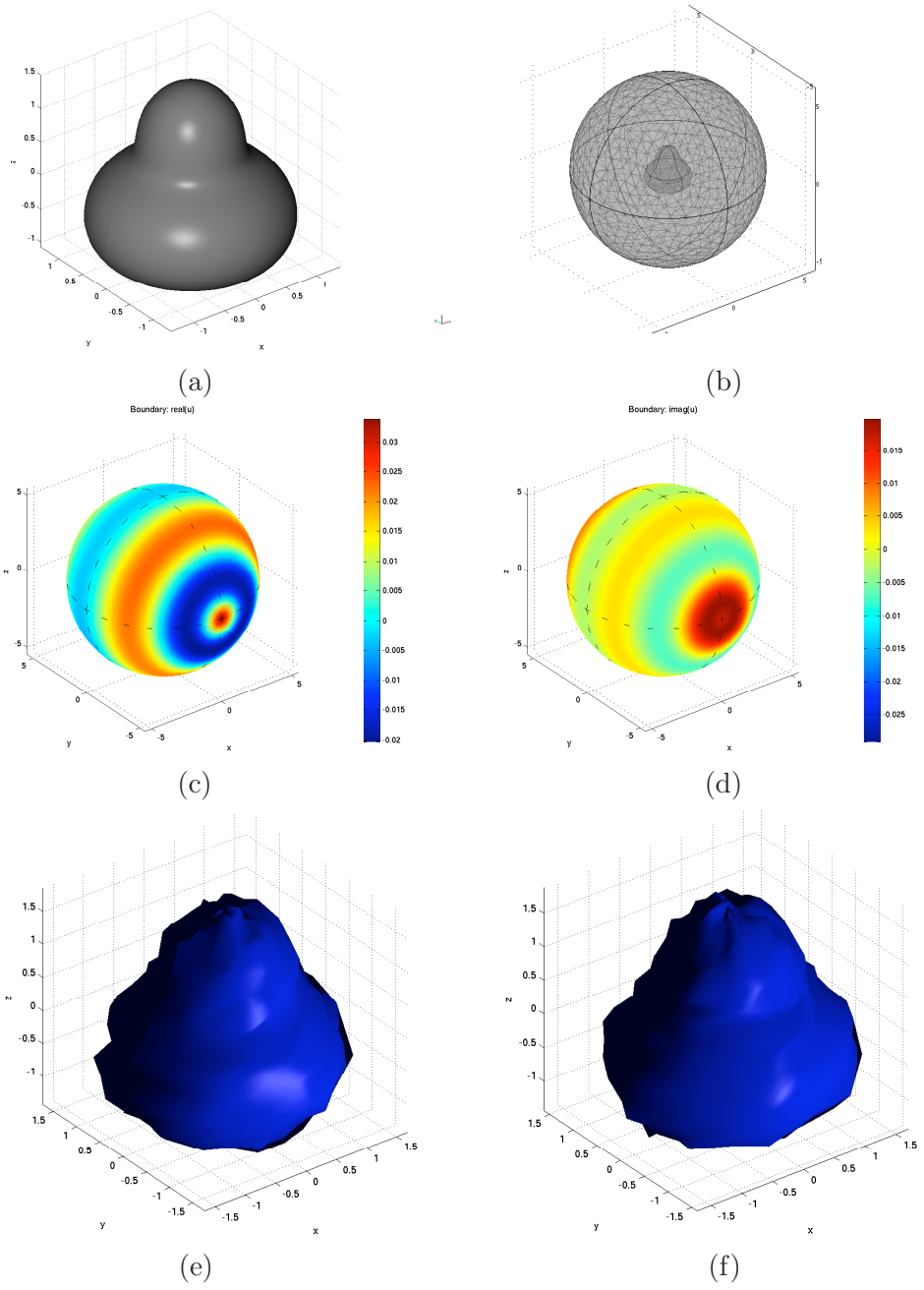

Figure 12: Example 5 with the singular point source. Exact shape of the acorn (a) and triangulation (b). Observed data u on the boundary of the surrounding sphere in real (c) and imaginary (d) parts when the singular source is located at $y = (-R_1, 0, 0)$. Reconstructed obstacles from the g-norm (e) ($V_{cut} = 0.098$) and res-norm (f) ($V_{cut} = -0.632$), respectively.

[10] Colton, D., Haddar, H. and Piana, M. *The linear sampling method in inverse electromagnetic inverse scattering theory*, Inverse Problems, **19** (2003), S105-37

[11] Colton, D. and Kirsch, A., *A simple method for solving inverse scattering problems in the resonance region*, Inverse Problems, **12** (1996), 383.

[12] Colton, D. and Kress, R., *Inverse Acoustic and Electromagnetic Scattering Theory*, 2nd edition, Springer-Verlag, New York, 1998.

[13] Colton, D. and Kress, R., *Using fundamental solutions in inverse scattering*, Inverse Problems, **22** (2006), R49.

[14] D. Colton and P. Monk, *The numerical solution of the three-dimensional inverse scattering problem for time harmonic acoustic waves*, SIAM J. Sci. and Stat. Comput., 8 (1987), pp. 278–291.

[15] Colton, D. and Monk, P., *A linear sampling method for the detection of leukemia using microwaves*, SIAM J. Appl. Math., **58** (1998), 926–941.

[16] Colton, D. and Sleeman, B. D., *An approximation property of importance in inverse scattering theory*, Proceedings of the Edinburgh Mathematical Society, **44** (2001), 449–544.

[17] Dos Santos Ferreira, D., Kenig, C. E., Sjöstrand, J. and Uhlmann, G., *Determining a magnetic Schrödinger operator from partial Cauchy data*, Commu. Math. Phys., **271** (2007), 467–488.

[18] Gebauer, B., Hanke, M., Kirsch, A., Muniz, W. and Schneider, C., *A sampling method for detecting buried objects using electromagnetic scattering*, Inverse Problems, **21** (2005), 2035–2050.

[19] Gilbarg, D. and Trudinger N. S., *Elliptic Partial Differential Equations of Second Order*, Springer, 2001.

[20] Ide, T., Isozaki, H., Nakata, S., Siltanen, S. and Uhlmann, G., *Probing for electrical inclusions with complex spherical waves*, Commu. Pure. Appl. Math., **60** (2007), 1415–1442.

[21] Ikehata, M. and Itou, H., *Extracting the support function of a cavity in an isotropic elastic body from a single set of boundary data*, Inverse Problems, **25** (2009), 105005.

[22] Ikehata, M., *Enclosing a polygonal cavity in a two-dimensional bounded domain from Cauchy data*, Inverse Problems, **15** (1999), 1231–1241.

[23] Ikehata, M., *How to draw a picture of an unknown inclusion from boundary measurements. Two mathematical inversion algorithms*, J. Inv. Ill-posed Problems, **7** (1999), 255–271.

[24] Isakov, V., *Inverse Problems for Partial Differential Equations*, New York: Springer, 2n ed., 2006.

[25] Kirsch, A. and Grinberg, N., *The Factorization Method for Inverse Problems*, Oxford University Press, 2008.

[26] Li J., Liu H., and Zou J., *Multilevel linear sampling method for inverse scattering problems*, SIAM J. Sci. Comp., **30** (2009), 1228–1250.

[27] Li J., Liu H., and Zou J., *Strengthened linear sampling method with a reference ball*, SIAM J. Sci. Comp., **31** (2009), 4013–4040.

[28] Li J., Liu H., Sun H., and Zou J., *Reconstructing Acoustic Obstacle By Planar and Cylindrical Waves.*

[29] Mclean, W., *Strongly Elliptic Systems and Boundary Integral Equations.* Cambridge University Press, 2000

[30] Nakamura, G. and Yoshida, K., *Identification of a non-convex obstacle for acoustical scattering*, J. Inv. Ill-posed Problems, **15** (2007), 611–624.

[31] Potthast, R., *A fast new method to solve inverse scattering problem*, Inverse Problem, **12** (1996) 731-742

[32] Potthast, R., *A point-source method method for inverse acoustic and electromagnetic obstacle scattering problems.* IMA Jour.Appl.math, **61** (1998) 119-140

[33] Potthast, R., *Point Sources and Multipoles in Inverse Scattering Theorey*, Chapman& Hall/CRC Research Notes in Math., 2001.

[34] Potthast, R., *A survey on sampling and probe methods for inverse problems*, Inverse Problems, **22** (2006), R1.

[35] Hongwei CHeng, William Y.Crutchfield, Zydrunas Gimbutas, Leslie F.Greengard, J.Frank Ethridge, Jingfang Huang, Vladimir Rokhlin, Norman Yarvin, Junsheng Zhao, *A Wideband Fast Multipole Method for the Helmholtz Equation in Three Dimension.* Journal of Computational Physics **216**(2006) 300-325

[36] P.A. Martin, *Multiple Scattering:Interaction of Time-Harmonic Waves with N Obstacles(Encyclopedia of Mathematics and its Applications).* Cambridge University Press, 2006

Research Reports

No.	Authors/Title
11-40	*J. Li, H. Liu, H. Sun and J. Zou* Imaging acoustic obstacles by hypersingular point sources
11-39	*U.S. Fjordholm, S. Mishra and E. Tadmor* Arbitrarily high order accurate entropy stable essentially non-oscillatory schemes for systems of conservation laws
11-38	*U.S. Fjordholm, S. Mishra and E. Tadmor* ENO reconstruction and ENO interpolation are stable
11-37	*C.J. Gittelson* Adaptive wavelet methods for elliptic partial differential equations with random operators
11-36	*A. Barth and A. Lang* Milstein approximation for advection–diffusion equations driven by multiplicative noncontinuous martingale noises
11-35	*A. Lang* Almost sure convergence of a Galerkin approximation for SPDEs of Zakai type driven by square integrable martingales
11-34	*F. Müller, D.W. Meyer and P. Jenny* Probabilistic collocation and Lagrangian sampling for tracer transport in randomly heterogeneous porous media
11-33	*R. Bourquin, V. Gradinaru and G.A. Hagedorn* Non-adiabatic transitions near avoided crossings: theory and numerics
11-32	*J. Šukys, S. Mishra and Ch. Schwab* Static load balancing for multi-level Monte Carlo finite volume solvers
11-31	*C.J. Gittelson, J. Könnö, Ch. Schwab and R. Stenberg* The multi-level Monte Carlo Finite Element Method for a stochastic Brinkman problem
11-30	*A. Barth, A. Lang and Ch. Schwab* Multi-level Monte Carlo Finite Element method for parabolic stochastic partial differential equations
11-29	*M. Hansen and Ch. Schwab* Analytic regularity and nonlinear approximation of a class of parametric semilinear elliptic PDEs
11-28	*R. Hiptmair and S. Mao* Stable multilevel splittings of boundary edge element spaces
11-27	*Ph. Grohs* Shearlets and microlocal analysis